We are IntechOpen,
the world's leading publisher of Open Access books
Built by scientists, for scientists

6,900
Open access books available

186,000
International authors and editors

200M
Downloads

154
Countries delivered to

Our authors are among the

TOP 1%
most cited scientists

12.2%
Contributors from top 500 universities

BOOK CITATION INDEX
CLARIVATE ANALYTICS
INDEXED

WEB OF SCIENCE™

Selection of our books indexed in the Book Citation Index
in Web of Science™ Core Collection (BKCI)

Interested in publishing with us?
Contact book.department@intechopen.com

Numbers displayed above are based on latest data collected.
For more information visit www.intechopen.com

LES of Unsteady Aerodynamic Forces on a Long-Span Curved Roof

Wei Ding

Abstract

The present paper discusses the unsteady aerodynamic forces on long-span curved roofs by using large eddy simulation (LES). The forced vibration test in a turbulent boundary layer is simulated. The models are force vibrated in the first anti-symmetric mode to investigate the influences of a roof's vibration on the wind pressure and flow field around a vibrating roof. The characteristics of unsteady aerodynamic forces in a wider range of reduced frequency of vibration are also investigated. A comparison between the wind tunnel experiment and the LES indicates that the LES can be used effectively to evaluate the unsteady aerodynamic force.

Keywords: large eddy simulation, unsteady aerodynamics force, long-span curved roof, forced vibration test

1. Introduction

Wind-structure interaction is a critical consideration in the design of many structures in civil engineering, especially for structures being flexible and light, such as long-span bridges, high-rise buildings, and long-span roofs. Such structures are generally vulnerable to the dynamic wind actions because of low damping and frequency [1–4]. The wind-structure interaction induces unsteady aerodynamic forces, or motion-induced wind forces, which may affect the wind-induced response significantly [5, 6]. Therefore, the unsteady aerodynamic force is an important consideration in the design of long-span vaulted roofs. Uematsu and Uchiyama [7] conducted a series of wind tunnel tests using elastic models of a one-way type of suspended roof. The mechanism of the wind-induced vibrations and the effect of wind-roof interaction on the dynamic response were discussed. Daw and Davenport [8] carried out a forced vibration test on a semi-circular roof to investigate the dependence of unsteady aerodynamic forces on the turbulence intensity, wind speed, vibration amplitude, and geometric details of the roof.

Ohkuma *et al*. [9] investigated the mechanism of aeroelastic instability of long-span flat roofs using a forced vibration test in a wind tunnel. At present, long-span curved roofs are universally constructed. However, there is an insufficient research on unsteady aerodynamic forces on long-span curved roofs, and the characteristics of unsteady aerodynamic forces are not well understood. Therefore, it is necessary to investigate this problem further for proposing more reasonable methods of response analysis for these roofs.

In this chapter, we investigate the characteristics of unsteady aerodynamic forces acting on long-span curved roofs for improving the wind-resistant design method. The large eddy simulation (LES) is used to discuss the influences of a roof's vibration on the wind pressure and flow field around a vibrating roof. The characteristics of unsteady aerodynamic forces in a wider range of reduced frequency of vibration are also investigated. The results of LES are validated by comparing with the experimental results.

2. Unsteady aerodynamic force

This section is focused on the illumination of unsteady aerodynamic forces (motion-induced forces), which result from the wind-structure interaction. Fluctuating deflections of the structure may be excited by the turbulence in oncoming flow, or the wake instability caused by vortex shedding in the structural wake. The unsteady aerodynamic forces result from the modification of the flow as the structure vibrates or changes shape, in other words, the interaction of the wind flow and structure. These forces may lead to instability. The unsteady aerodynamic force is described as two components: the aerodynamic stiffness term that is in-phase with the displacement and the aerodynamic damping term that is out-phase with displacement.

The aerodynamic stiffness is the added stiffness of the air surrounding the structure, which may increase or effectively reduce available structural static stiffness. For a conventional heavy structure, the aerodynamic stiffness is generally insignificant in comparison to the structural stiffness. However, for a long-span light-weight structure, which vibrates more easily in the wind, the aerodynamic stiffness may change the structural response. For instance, if the total static stiffness of the system in wind is reduced to zero, then a divergent instability may be induced.

When a structure is vibrating in the wind, the relative velocity of the structure to the wind flow changes in magnitude and direction. This phenomenon effectively produces an added damping force, referred to as aerodynamic damping. The aerodynamic damping may add to the structural damping to reduce the response of structure, or become negative and increase the response of the structure. The chances of aerodynamic instability are high as the total damping in the system approaches zero.

2.1. Definition of unsteady aerodynamic force

The displacement of structure in the *j*th mode may be represented by the following equation,

$$Z_j(s,t) = \varphi_j(s)x_j(t) \tag{1}$$

where φ_j and x_j are the mode shape and generalized displacement of the *j*th mode, respectively; and *s* represents the circumferential coordinate taken along the roof.

Applying a modal analysis to the equation of motion for the roof, we obtain the following equation of motion for the jth generalized displacement,

$$M_{s_j}\ddot{x}_j(t) + C_{s_j}\dot{x}_j(t) + K_{s_j}x_j(t) = F_{W_j}(t) + F_{A_j}(t) \tag{2}$$

$$\ddot{x}_j(t) + 2\xi_{s_j}\omega_{s_j}\dot{x}_j(t) + \omega_{s_j}^2 x_j(t) = F_j(t)/M_{s_j} \tag{3}$$

$$F_j(t) = F_{W_j}(t) + F_{A_j}(x, \dot{x}, \ddot{x} \dots) \tag{4}$$

where M_{sj} = generalized mass, ω_{sj} = natural circular frequency, ζ_{sj} = critical damping ratio, and F_j = generalized force. F_{Wj} represents the fluctuating wind force due to the oncoming flow and wake instability, while F_{Aj} represents the unsteady aerodynamic force due to the wind-roof interaction.

In the case of the forced-vibration test, a steady vibration in the first anti-symmetric mode represented by a sine curve is applied to the roof. The unsteady aerodynamic force F_{Aj} (here $j = 1$) can be obtained from Eq. (5) by using the Fourier series at the frequency f_m of the forced vibration:

$$F_{A_j}(t) = F_{R_j}\cos 2\pi f_m t - F_{I_j}\sin 2\pi f_m t \tag{5}$$

$$F_{R_j} = \frac{1}{T}\int_{-T}^{T} F_j(t)\cos 2\pi f_m t \tag{6}$$

$$F_{I_j} = \frac{1}{T}\int_{-T}^{T} F_j(t)\sin 2\pi f_m t \tag{7}$$

where F_{Rj} and F_{Ij} are the in-phase and out-of phase components of the unsteady aerodynamic force, respectively.

3. Large eddy simulation

The LES is used to investigate the characteristics of unsteady aerodynamic forces. The influences of a roof's vibration on the wind pressure and flow field around a vibrating roof are also investigated. The simulation is carried out by using a CFD software 'STAR-CD'.

3.1. Computational outline

3.1.1. Computational model

The computational model used in the 'STAR-CD' is shown in **Figure 1**. In order to investigate the effect of geometric shape on the unsteady aerodynamic force, the rise/span ratio r/L of computational models is assumed to be 0.15, 0.20, and 0.25. The curved roof model is forced to vibrate in the first anti-symmetric mode as shown in **Figure 1**.

3.1.2. Computational parameters

Table 1 summarizes the computational parameters. In order to discuss the effect of geometric shape on wind-roof interaction, the rise/span ratio is changed from 0.15 to 0.25. The amplitude
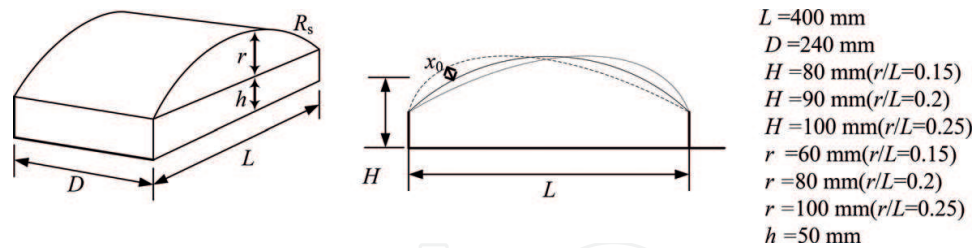
L =400 mm
D =240 mm
H =80 mm(r/L=0.15)
H =90 mm(r/L=0.2)
H =100 mm(r/L=0.25)
r =60 mm(r/L=0.15)
r =80 mm(r/L=0.2)
r =100 mm(r/L=0.25)
h =50 mm

Figure 1. Computational model.

Wind speed	5 m/s
Forced vibration amplitude	4 mm
Rise/span ratio (r/L)	0.15, 0.20, 0.25
Forced vibration frequency (f_m)	0–160 Hz (10 Hz increment)
Reduced vibration frequency(f_m^*)	0–2.5

Table 1. Parameter of CFD simulation.

x_0 of vibration is fixed to 4.0 mm (i.e. $x_0/L = 1/100$). In this study, based on the assumptions of the mean roof height for real structure $H_r = 20$ m; the wind speed at mean roof height $U_{H\_r} = 20$–40 m/s; the natural frequency $f_s = 0.4$–2.5 Hz. We calculated the reduced frequency for real roof $f_r^* = 0.2$–2.5, as shown in **Table 3**. In order to satisfy the similarity principle of real long-span roofs $f_m^* = f_r^*$ (f_m^* = the reduced frequency for model), the forced vibration frequency f_m should be set at 12.5–156.25 Hz, as shown in **Table 2**. With regard to the limitation of forced vibration equipment used in the wind tunnel experiment [10], the forced vibration
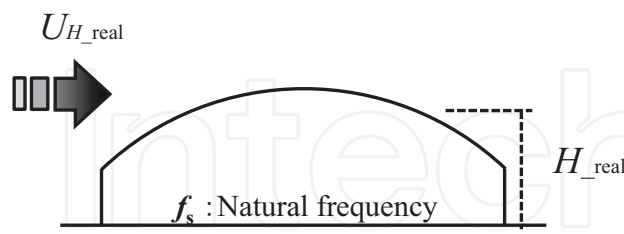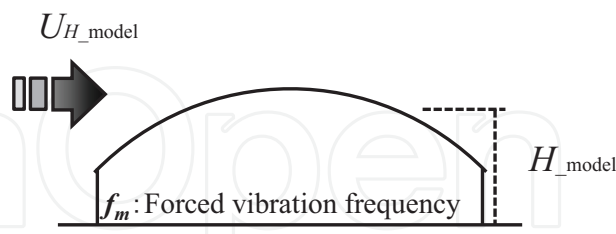

$$f_{\_r}^* = \frac{f_s H_{\_r}}{U_{H\_r}}$$

Mean roof height for real structure $H_{\_r} = 20$ m

Wind speed at mean roof height $U_{H\_r} = 20$–40 m/s

Natural frequency $f_s = 0.4$–2.5 Hz

Reduced frequency for real roof $f_{\_r}^* = 0.2$–2.5

$$f_m^* = \frac{f_m H}{U_H}$$

Mean roof height for model $H = 0.08$ m

Wind speed at mean roof height $U_H = 5$ m/s

Forced vibration frequency $f_m = 12.5$–156.25 Hz

Reduced frequency for model $f_m^* = f_{\_r}^* = 0.2$–2.5

Table 2. Determination of forced vibration frequency.

frequency cannot be set as large as this. Therefore, it is necessary to use LES to examine the characteristics of unsteady aerodynamic forces in a wider range of reduced frequency. For the LES, we change the forced vibration frequency from 0 to 160 Hz and the range of reduced frequency of vibration is from 0 to 2.5, as shown in **Table 1**.

3.1.3. Computational domain

Figure 2 shows the computational domain. In this study, the length of span direction equals the span of roof to generate two-dimensional flow that is corresponded with that used in the wind tunnel experiment.

3.1.4. Computational mesh

In the simulation, various types of mesh arrangements were calculated. We compared the results of LES with those of wind tunnel experiment. And then, the mesh arrangement was selected which leads to the most corresponding results with that of experiment, as shown in **Figure 3**. The magnitude of minimum mesh is 0.15×10^{-3}. And the dynamic mesh is used to simulate the vibration of model.
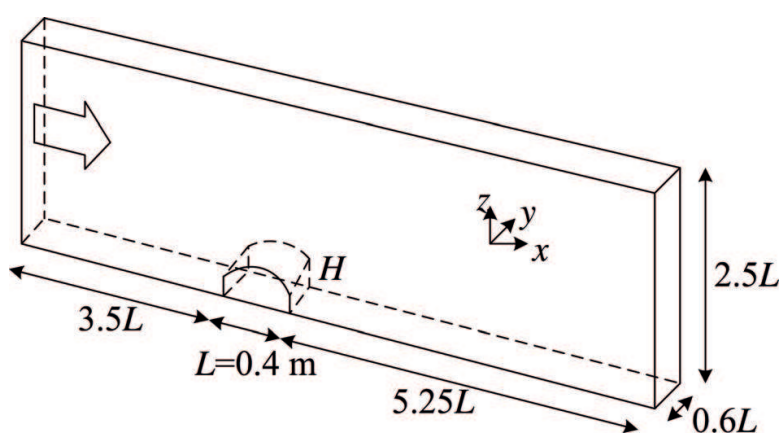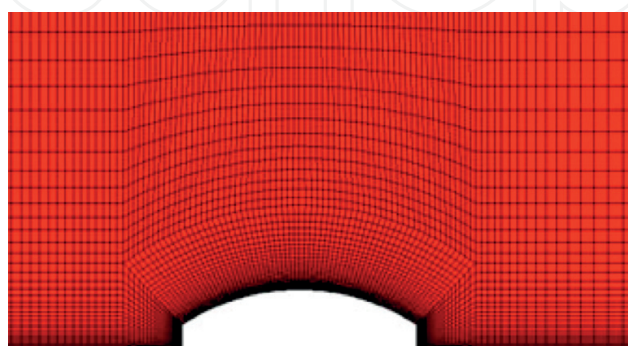

Figure 2. Computational domain.

Figure 3. Mesh arrangement around roof.

3.1.5. Computational and boundary conditions

There are mainly three types of CFD approaches, which are used in computational wind engineering (CWE): the Reynolds-averaged Navier-Stokes (RANS), the large eddy simulations (LES), and direct numerical simulation (DNS). Due to the limitation of available computer memory and speed at present, DNS cannot be widely used in CWE for solving complicated practical problems. RANS solves the time-averaged NS equations, and the averaged solution reflects the averaged properties of the turbulent flow. Thus, the time-averaged solution is less trustable in nonstationary flows. On the other hand, LES resolves the scale of motion larger than the gird size and the effect of motion of turbulent eddy smaller than grid scale needs to be modeled. The unsteady motions of large eddy can be explicitly predicted and the accuracy is usually much better than RANS models, since the effects of only small eddy are modeled. Therefore, the LES is adopted in this study.

The governing equations adopted in the present LES method are the spatially filtered continuity and Navier-Stokes equations as follows,

$$\frac{\partial \overline{u}_i}{\partial x_i} = 0 \tag{8}$$

$$\frac{\partial \overline{u}_i}{\partial t} + \frac{\partial \overline{u}_i \overline{u}_j}{\partial x_j} = -\frac{1}{\rho}\frac{\partial \overline{p}}{\partial x_i} + \frac{\partial}{\partial x_j}\left(\nu\frac{\partial \overline{u}_i}{\partial x_j}\right) - \frac{\partial \tau_{ij}}{\partial x_i} \tag{9}$$

$$\tau_{ij} = \overline{u_i u_j} - \overline{u_i}\,\overline{u_j} \tag{10}$$

where u_i, u_j represent flow velocity in i-direction and j-direction. The p, ρ, and ν represent pressure, density, and dynamic viscosity of the fluid, respectively. The ($\overline{u}$) denotes application of the spatial filter. The τ_{ij} is subgrid-scale (SGS) stress, which is parameterized by an eddy viscosity model. The standard Smagorinsky model is adopted to estimate the term of τ_{ij}, as shown in Eqs. (11)–(13).

$$\tau_{ij} = -2\nu_{SGS}\overline{S}_{ij} + \frac{1}{3}\delta_{ij}R_{kk} \tag{11}$$

$$\overline{S}_{ij} = \frac{1}{2}\left(\frac{\partial \overline{u}_i}{\partial x_j} + \frac{\partial \overline{u}_j}{\partial x_i}\right) \tag{12}$$

$$\nu_{SGS} = \left(C_s\overline{\Delta}\right)^2\sqrt{2\overline{S}_{ij}\overline{S}_{ij}} \tag{13}$$

where ν_{SGS} is the subgrid-scale turbulent eddy viscosity. $\overline{S}_{ij}$ is the rate of strain tensor for the resolved scale. Δ means the spatial filter width and C_s is the Smagorinsky constant and is taken as 0.12 ($C_s = 0.12$). The computational and boundary conditions are summarized in **Table 3**.

Computational domain	$9.75L(x) \times 0.6L(y) \times 2.5L(z)$
Inlet boundary	Inflow turbulence is generated in preliminary computational domain
Upper boundary	Zero normal velocity and zero normal gradients of other variables
Side boundary	Cyclic boundary conditions
Outlet boundary	Zero normal gradients of all variables
Floor and model surfaces	No-slip condition
Grid discretization	$260(x) \times 24(y) \times 64(z) = (399, 360)$
Convection schemes	Second-order centered difference scheme
Time differential schemes	Euler implicit
Numerical algorithm	PISO algorithm
Time	$T = 4$ s, $\Delta t = 2.0E-04$ s (Courant Number: 9.1E−02)

Table 3. Computational and boundary conditions.

3.1.6. Inflow turbulence

As is known, the flow around a structure is strongly affected by the flow turbulence. Therefore, the proper generation of the inflow turbulence for the LES is essential in the determination of wind loads on structures. At present, several techniques have been developed. In general, there are three kinds of inflow turbulence generation methods. The first approach is to store the time history of velocity fluctuations obtained from a preliminary LES computation. Nozu and Tamura [11] employed the interpolation method with the periodic boundary condition to simulate a fully developed turbulent boundary layer and tried to change the turbulent characteristics by using roughness blocks. Another approach is to numerically simulate the turbulent flow in auxiliary computational domains (often called a driver region set at the upstream region of a main computational domain). Lund *et al*. [12] proposed the method to generate turbulent inflow data for the LES of a spatially developing boundary layer. Kataoka and Mizuno [13] simplified Lund's method by assuming that the boundary layer thickness is constant within the driver region, and only the fluctuating part of velocity is recycled in the streamwise direction. Nozawa and Tamura [14, 15] discussed the potential of large eddy simulation for predicting turbulence characteristics in a spatially developed turbulent boundary layer over a rough ground surface and improved Lund's method. The third approach is to use artificial numerical models to generate inflow turbulence statistically [16–19].

In this study, we use a preliminary LES to simulate inflow turbulence and store the time history of velocity fluctuations. **Figure 4** shows a schematic illustration of the domain of the preliminary computation. In the domain, the roughness blocks with heights 3, 5, and 8 cm are distributed on the ground to generate turbulence. The computational and boundary conditions are summarized in **Table 4**.
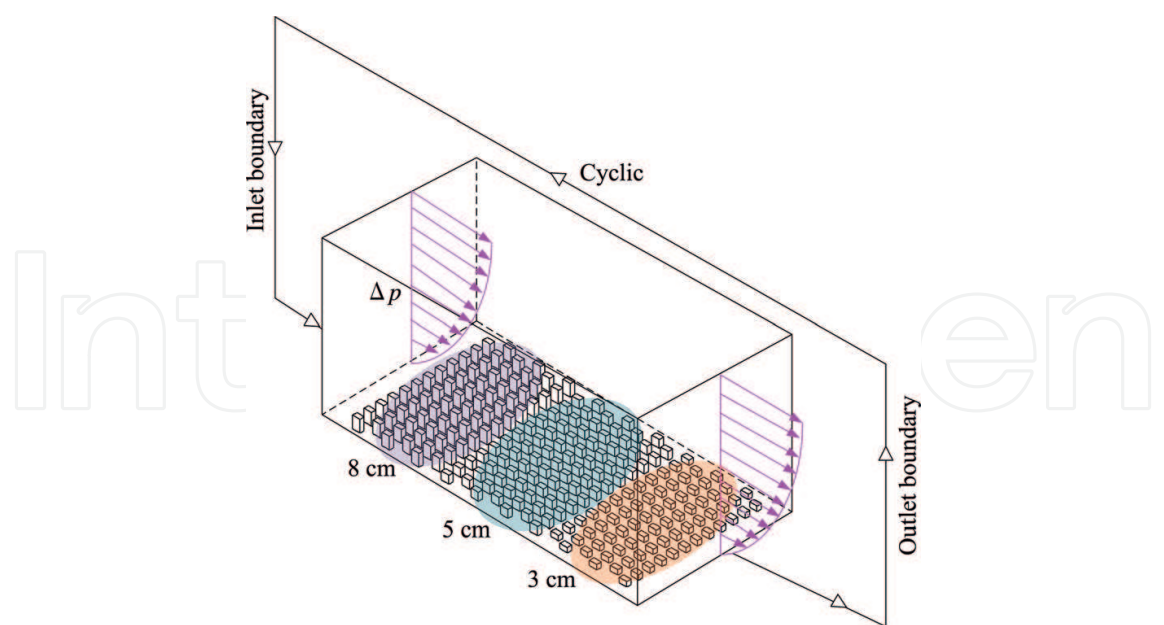
Figure 4. Preliminary computational domain.

Inlet boundary	Cyclic boundary condition
Upper boundary	Zero normal velocity and zero normal gradients of other variables
Side boundary	Cyclic boundary conditions
Outlet boundary	Cyclic boundary conditions
Floor and surfaces of roughness blocks	No-slip condition
Convection schemes	MARS method
Diffusion schemes	Centered difference scheme
Time differential schemes	First order Euler implicit
Numerical algorithm	PISO algorithm
Time step	$\Delta t = 2.0\text{E}{-}04$ s

Table 4. Computational and boundary conditions.

The profiles of the mean wind speed and turbulent intensity at the inlet of the computational domain are shown in **Figure 5(a)**. The longitudinal velocity spectrum at a height of $H = 90$ mm is shown in **Figure 5(b)**. In both figures, the results of wind tunnel flow are also plotted for comparative purposes. It can be seen that the inflow turbulence used in the LES is generally in good agreement with that used in the wind tunnel experiment.
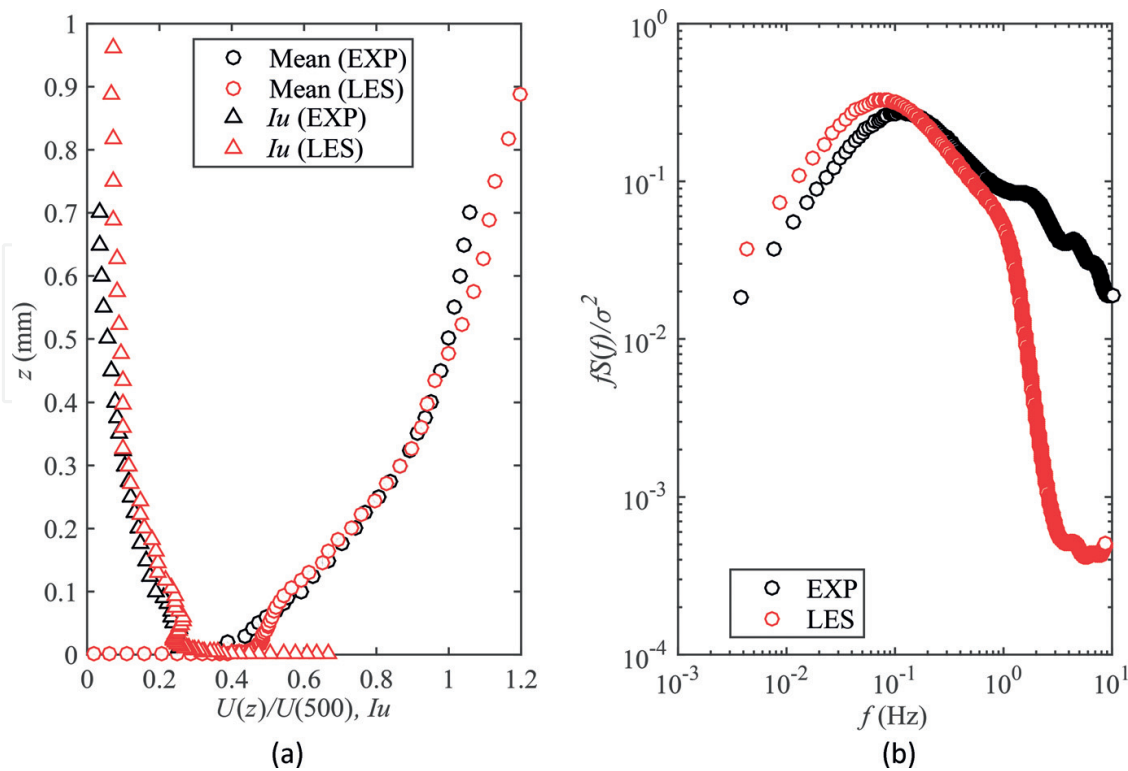
Figure 5. Comparison of inflow turbulence between wind tunnel experiment and LES; (a) profiles of mean wind speed ($U(z)$) and turbulence intensity (Iu); (b) longitudinal velocity spectrum ($H = 90$ mm).

4. Results and discussion

4.1. Comparison with wind tunnel experiment

In order to validate the LES computation, the distributions of the mean wind pressure coefficient C_{p_mean} and fluctuating wind pressure coefficient C_{p_RMS} along the centerline of the vibrating roof is compared with those obtained from the wind tunnel experiment. **Figures 6** and **7** show the results, in which the results for the frequencies of 0, 10, and 15 Hz are plotted. It can be seen that there is generally a good agreement between the LES and the wind tunnel experiment. In **Figure 6**, the difference is somewhat larger near the rooftop; the LES values are approximately 10% larger in magnitude than the experimental ones. This difference may be due to a difference in surface roughness of the roof between the LES and the wind tunnel experiment. In **Figure 7**, when the $f_m = 0$ Hz, the value of C_{p_RMS} for the LES is larger than that for the wind tunnel test. That maybe because that the turbulence intensity of inflow turbulence used in the LES is slightly larger than that used in the wind tunnel test (see **Figure 5**).

4.2. Distribution of wind pressure on the roof

The distributions of mean and rms fluctuating wind pressure coefficients for various forced-vibration frequencies are shown in **Figure 8**. It can be seen that the mean wind pressure
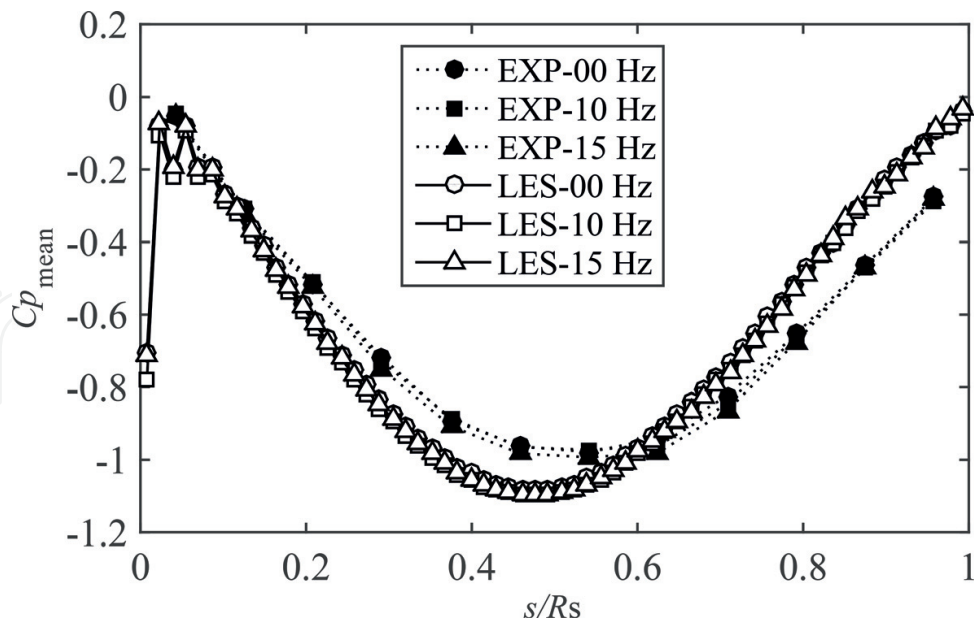
Figure 6. Comparisons for the distribution of the mean wind pressure coefficients along the centerline between LES and wind tunnel experiment.
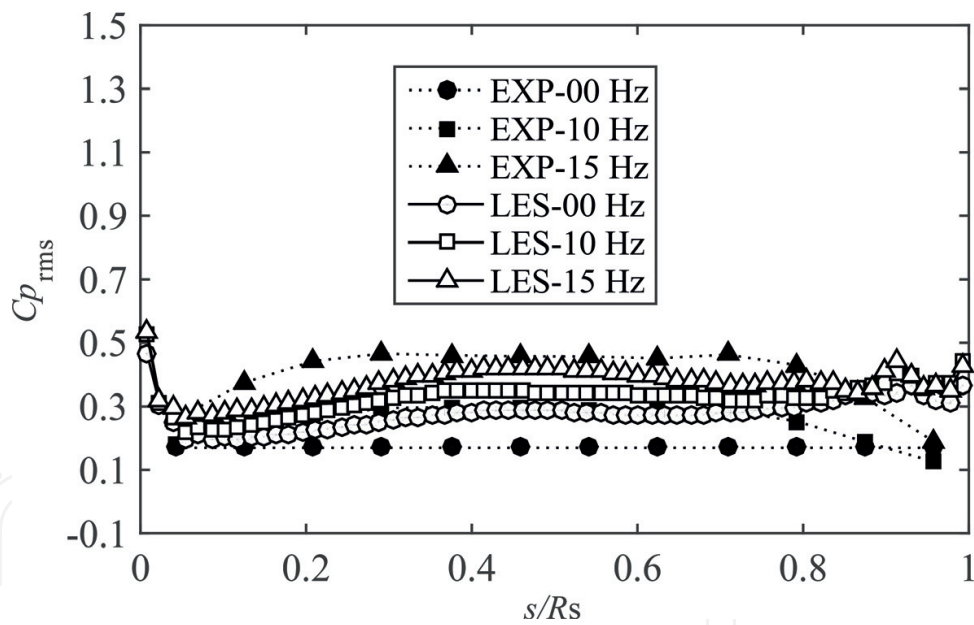

Figure 7. Comparisons for the distribution of the fluctuating wind pressure coefficients along the centerline between LES and wind tunnel experiment.

coefficients *Cp_mean* near the rooftop increase in magnitude and the rms fluctuating wind pressure coefficients *Cp_rms* generally increase, as the forced-vibration frequency increases. Furthermore, the variation is significant near the position of the greatest forced-vibration amplitude. These results indicate that the wind pressure field around the vibrating roof is strongly influenced by the vibration of the roof.
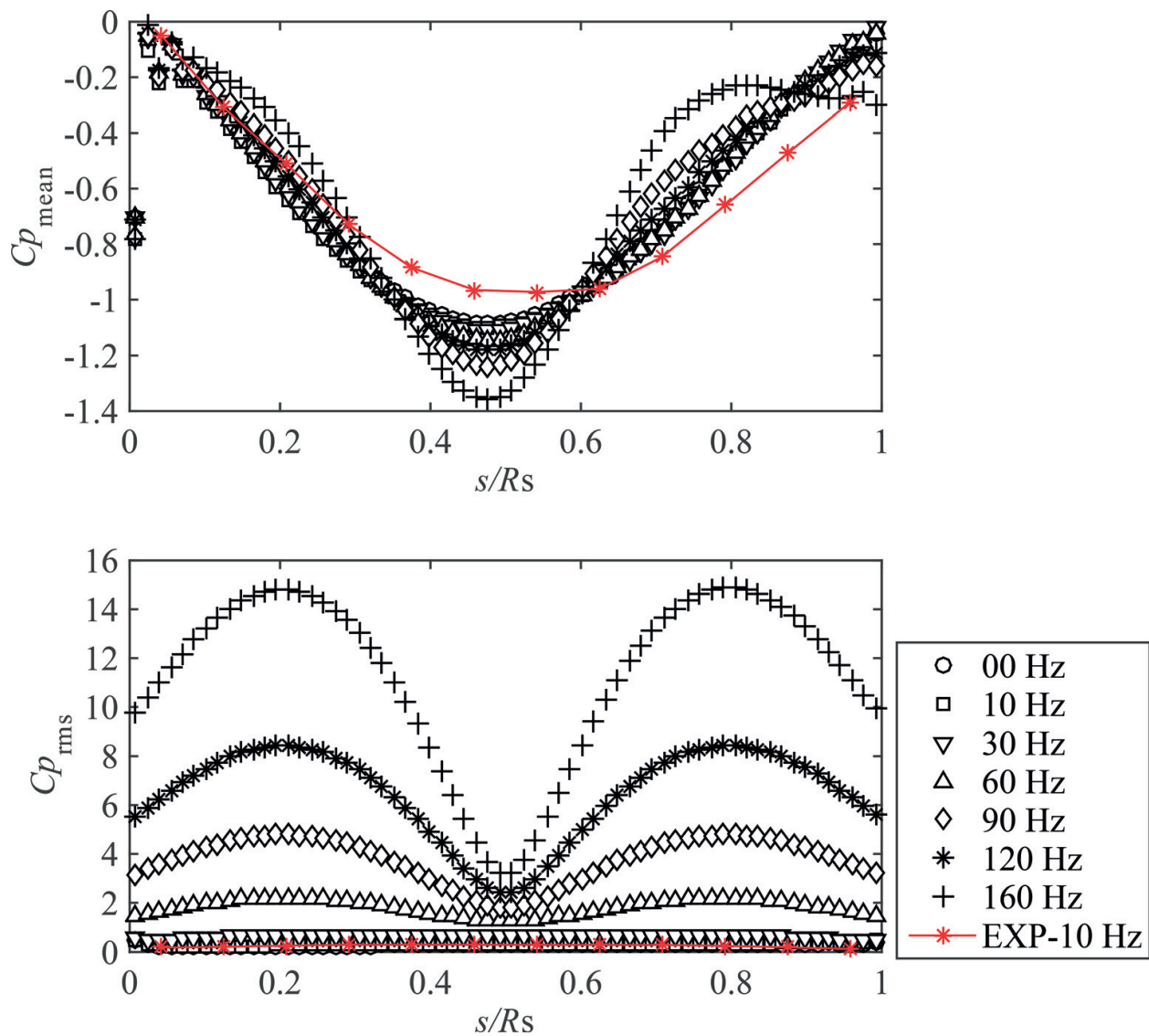
Figure 8. Variation of mean and fluctuating wind pressure coefficients with forced vibration frequency (r/L = 0.15).

Figure 9 shows the variations of mean and rms fluctuating wind pressure coefficients with the rise/span ratio. It can be seen that the *Cp_mean* changes from negative to positive at the leading edge of the roof as the rise/span ratio increases. Furthermore, the negative peak value increases in magnitude with an increase in rise/span ratio. The value of *Cp_rms* increases with an increase in rise/span ratio at the middle part of the roof. However, the effect of *r/L* on *Cp_rms* is less significant than on *Cp_mean*.

4.3. Discussion flow field around the roof

The roof configurations at several steps (phases) during one period of vibration are shown in **Figure 10**. The deformation of the windward side is upward and becomes the greatest at step 2; and that of the leeward side is upward and becomes the greatest at step 4.
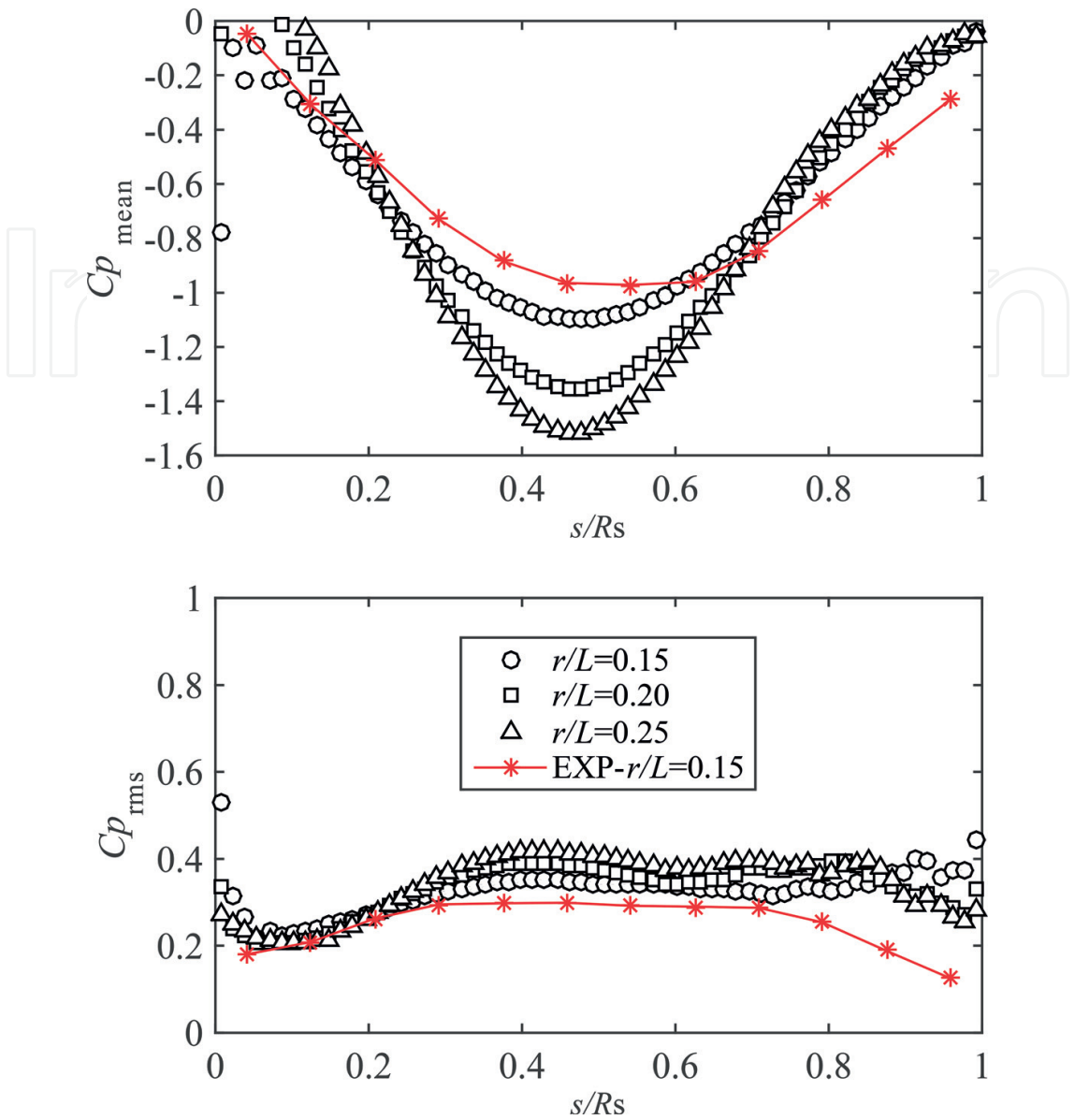
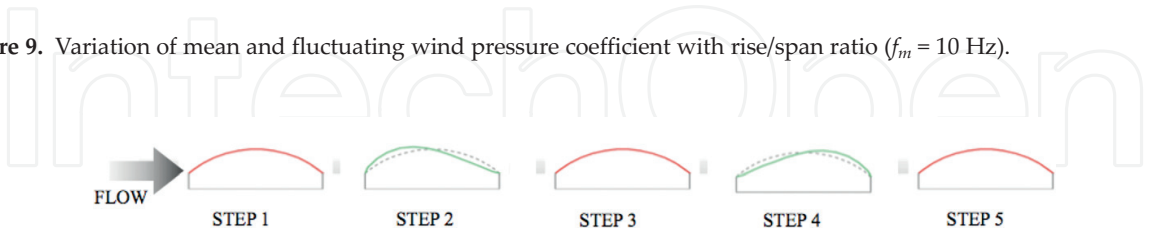**Figure 9.** Variation of mean and fluctuating wind pressure coefficient with rise/span ratio (f_m = 10 Hz).

Figure 10. Roof configurations at several steps.

Figure 11 shows representative flow fields around a stationary or vibrating roof at a frequency of 10 or 20 Hz. It can be seen that the wind speed increases near the roof regardless of the roof's vibration. In the case of a stationary roof (f_m = 0 Hz), the flow separates near the 3/4 position of the roof from the leading edge. On the other hand, in the case of a vibrating roof, the separated vortex seems smaller than that in the stationary roof case, which may be due to the vibration of the roof that restrains the separation of the vortex. In addition, the separated position at the
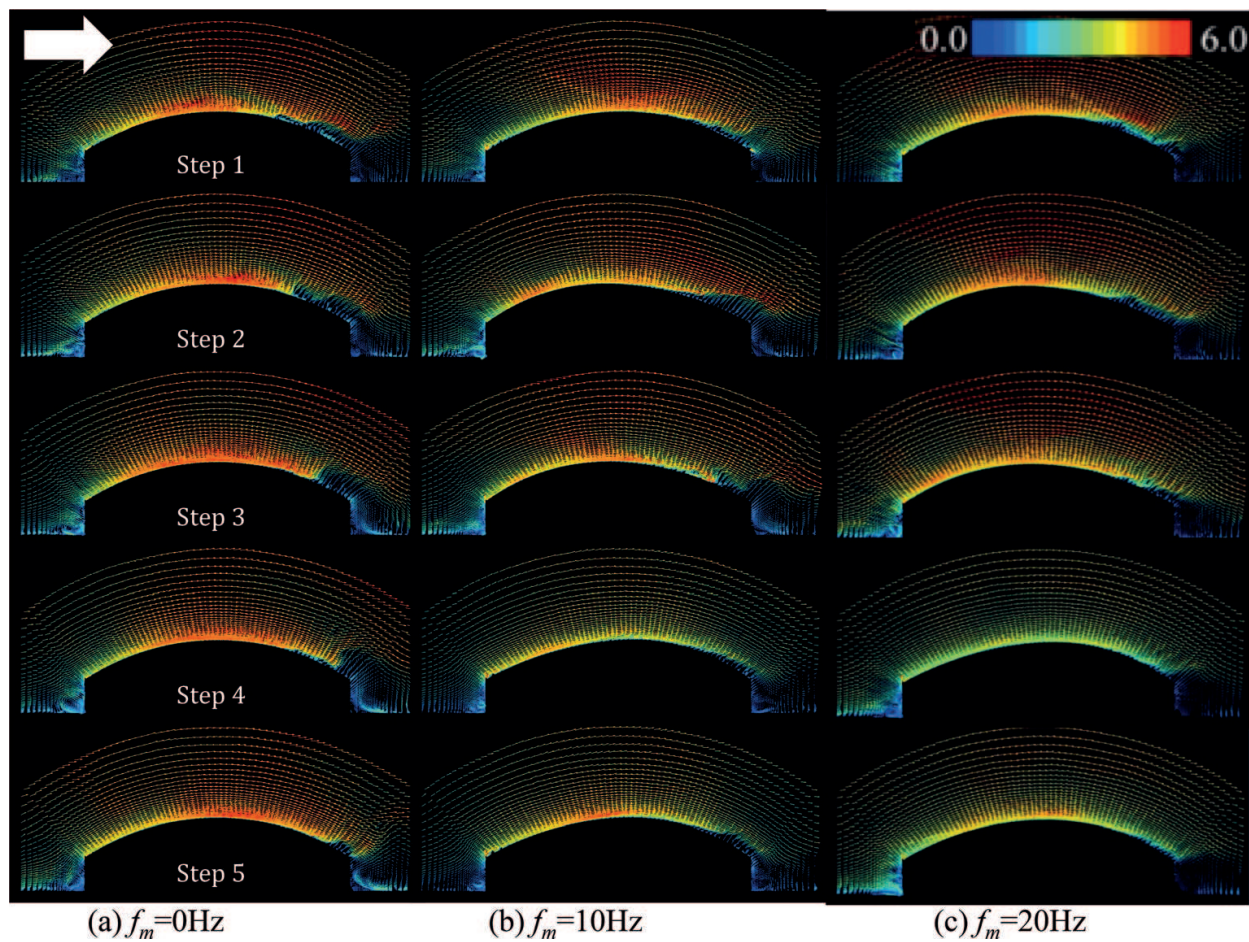
Figure 11. Flow fields around the roof for various forced vibration frequencies (r/L = 0.15); (a) 0 Hz; (b) 10 Hz; (c) 20 Hz.

rear of roof changes with the vibration of roof. The separated position is relatively forward when the roof is vibrated in step 1 to step 3, because the deformation at the windward side of roof makes the flow separated in advance. On the other hand, the separated position is relatively backward when the roof is vibrated in step 3 to step 5, as the result that the deformation at the leeward side of roof restrains the flow separated.

Figure 12 shows the effect of the rise/span ratio on the flow field around a vibrating roof at a forced vibration frequency of 20 Hz. It can be seen that the wind speed near the rooftop becomes higher, generating larger suction as the rise/span ratio increases. Therefore, the negative peak value of Cp_mean increases with an increase in rise/span ratio (see **Figure 8**). Furthermore, as the rise/span ratio increases, the vortex at the rearward of roof becomes larger. Flow fields around the roof for various rise/span ratios (f_m = 20 Hz); (a) r/L = 0.15; (b) r/L = 0.20; (c) r/L = 0.25.

4.4. Evaluation of unsteady aerodynamic forces

In this study, we use aerodynamic stiffness coefficient a_{Kj} and aerodynamic damping coefficient a_{Cj} to investigate the characteristics of unsteady aerodynamic forces acting on a vibrating long-span curved roof, which are given by the following equations [8]:
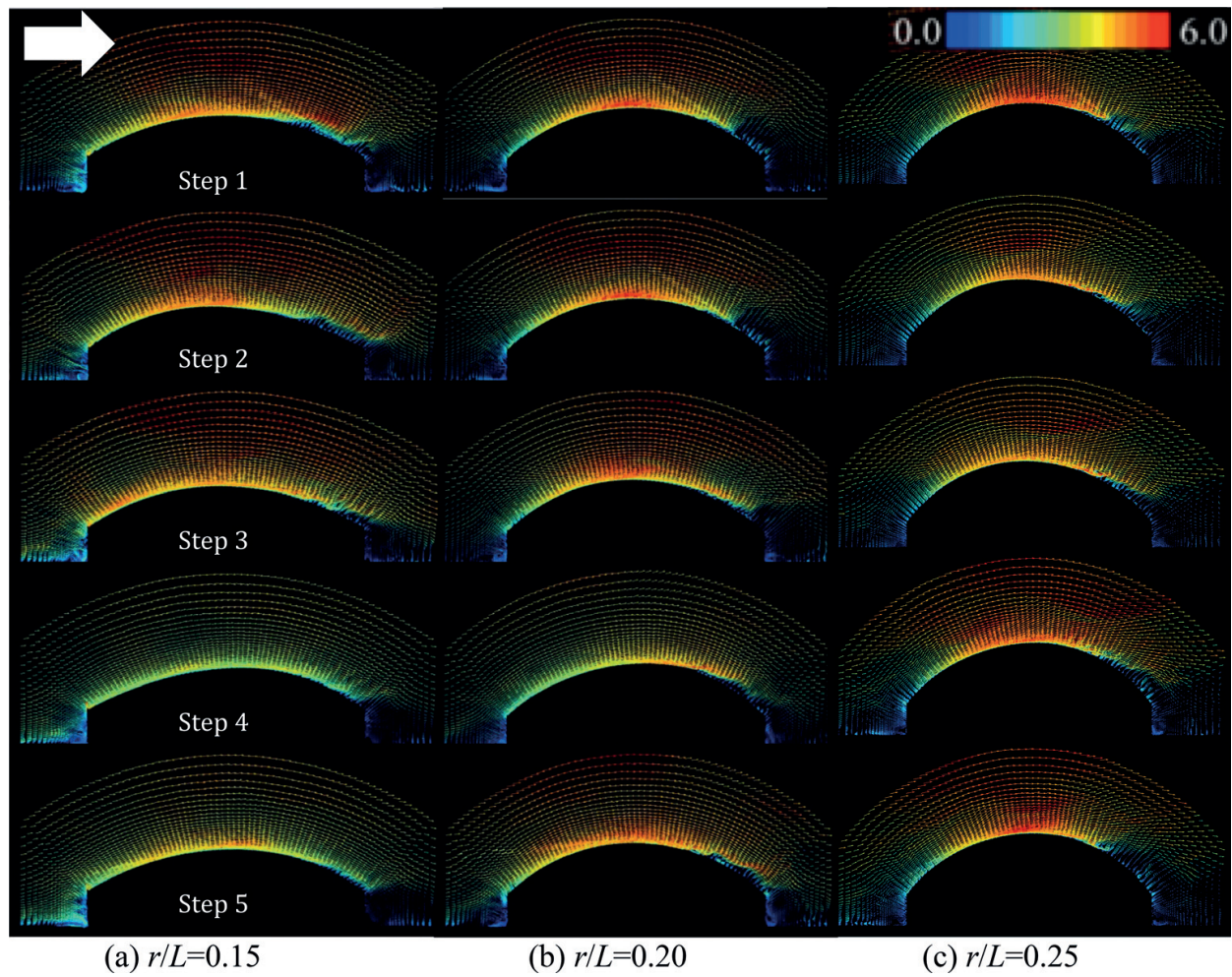
Step 1

Step 2

Step 3

Step 4

Step 5

(a) *r/L*=0.15   (b) *r/L*=0.20   (c) *r/L*=0.25

Figure 12. Flow fields around the roof for various rise/span ratios (f_m = 20 Hz); (a) r/L = 0.15; (b) r/L = 0.20; (c) r/L = 0.25.

$$a_{Kj} = \frac{F_{Rj}(f_m)}{q_H A_s (x_0/L)} = \frac{1}{q_H A_s (x_0/L)} \frac{1}{T} \int_{-T}^{T} F_j(t) \cos 2\pi f_m t \tag{14}$$

$$a_{Cj} = \frac{F_{Ij}(f_m)}{q_H A_s (x_0/L)} = \frac{1}{q_H A_s (x_0/L)} \frac{1}{T} \int_{-T}^{T} F_j(t) \sin 2\pi f_m t \tag{15}$$

where F_{Rj} is the in-phase component with the generalized displacement represented as the aerodynamic stiffness term, F_{Ij} is the in-phase component with velocity represented as the aerodynamic damping term, q_H = velocity pressure at the mean roof height H, A_s = roof area, x_0 = forced vibration amplitude, L = span of the roof, T = vibration period, f_m = forced vibration frequency, and $f_m{}^*$ = reduced frequency of vibration, defined by $f_m H/U_H$, with U_H being the mean wind speed at the mean roof height H.

The generalized force F_j may be described in terms of the external and internal pressures p_e and p_i, as shown in Eq. 16,

$$F_j(t) = \int_0^{R_s} \left[p_{e_j}(s, t) - p_{i_j}(s, t) \right] \varphi_j(s) ds \tag{16}$$

where R_s = total length of the vaulted roof. Internal pressure p_i is ignored in the present study, because the first anti-symmetric mode under consideration causes no change of internal volume. The model's vibration mode almost corresponded with the asymmetric sine mode, as shown in Eq. 17.

$$\varphi_j(s) = \sin 2\pi \frac{s}{R_s} \tag{17}$$

Figure 13 shows the aerodynamic stiffness and damping coefficients, a_K and a_C, obtained from the LES and the wind tunnel experiment, plotted as a function of the reduced frequency of vibration f_m^* ($f_m^* = f_m H/U_H$). The wind tunnel experiment was carried out in a limited range of f_m^*, while the LES was conducted over a wider range of f_m^*. It can be seen that the LES results are consistent with those of the wind tunnel experiment, which indicates that the LES model can be used for investigating the characteristics of unsteady aerodynamic forces. The aerodynamic stiffness coefficient a_K is generally positive and increases with an increase in f_m^*, which decreases the total stiffness of the system. On the other hand, the aerodynamic damping coefficient a_C is negative and increases in magnitude with an increase in f_m^*, resulting in an increase in the total damping of the system.

The distribution of aerodynamic stiffness and damping coefficients a_K and a_C with f_m^* for various rise/span ratios is shown in **Figure 14**. It can be seen that the values of a_K for $r/L = 0.15$, 0.20, and 0.25 are generally consistent with each other when $f_m^* < 0.4$. However, when $f_m^* > 0.4$, the value of a_K decreases with an increase in the rise/span ratio. Regarding the value of a_C, the results for various rise/span ratios are generally similar to each other. This figure indicates that the value of a_K is influenced by the rise/span ratio of a long-span vaulted roof. However, the effect of the rise/span ratio on the value of a_C is small.
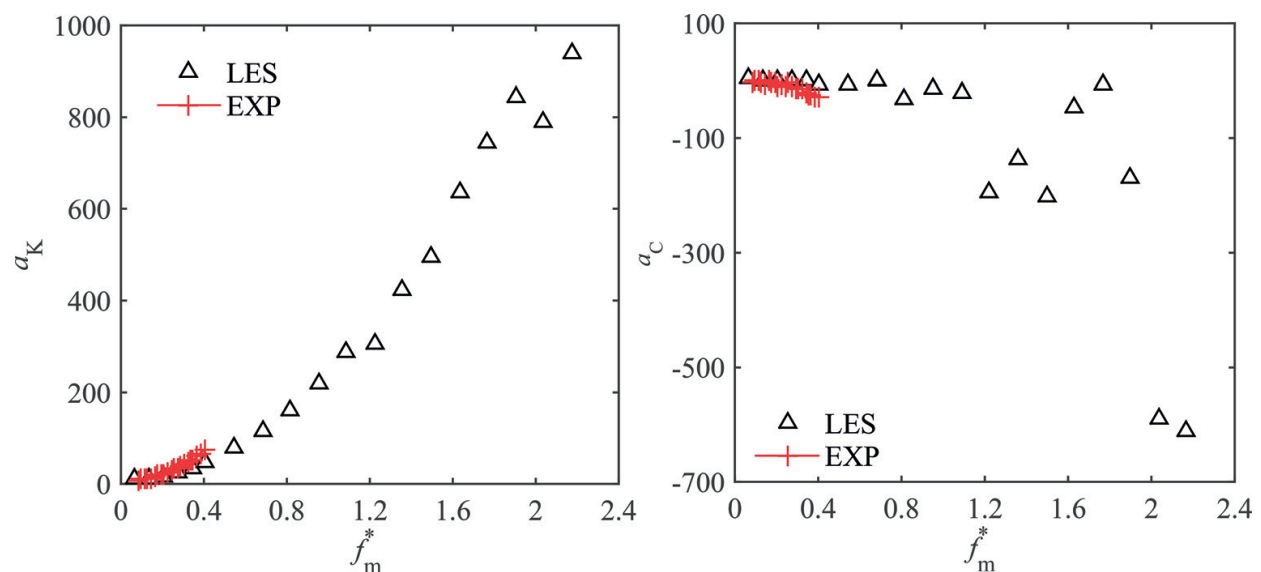

Figure 13. Comparisons of the LES and the wind tunnel experiment for the aerodynamic stiffness coefficient a_K and aerodynamic damping coefficient a_C versus reduced frequency of vibration f_m^*.
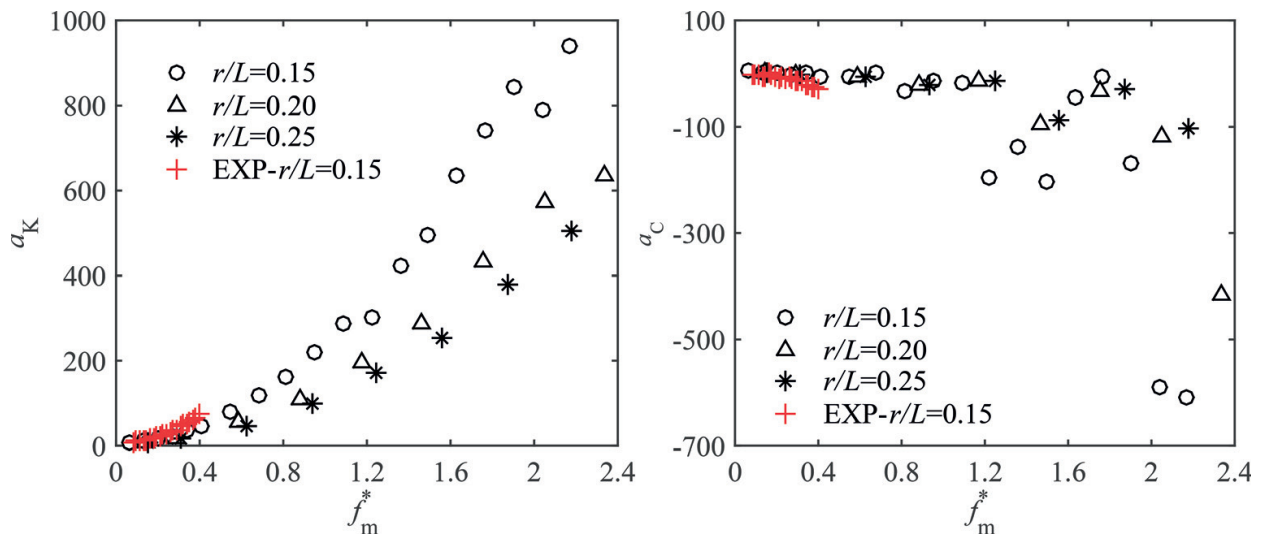
Figure 14. Aerodynamic stiffness and damping coefficients versus f_m^* for different rise/span ratio r/L.

5. Concluding remarks

The unsteady aerodynamic forces acting on the long-span curved roof have been investigated based on a numerical simulation (LES). A forced vibration test was carried out. First, the influence of a roof's vibration on the wind pressure was investigated. It is found that the wind pressure on a vibrating roof is strongly influenced by the roof's vibration. Furthermore, the flow field around a vibrating roof was also investigated. It is found that the vibration of the roof may restrain the separation of a vortex near the trailing edge of the roof. Finally, the characteristics of unsteady aerodynamic force acting on a long-span vaulted roof were evaluated. Both the wind tunnel experiment and CFD simulation show similar results for the variation of aerodynamic stiffness and damping coefficients a_K and a_C with reduced frequency of vibration f_m^*, which implies that the LES is effective to investigate the characteristics of unsteady aerodynamic forces. The aerodynamic stiffness coefficient is generally positive, which decreases the total stiffness of the system, resulting in aeroelastic instability of long-span vaulted roofs with lower stiffness. On the other hand, the aerodynamic damping coefficient is negative, which results in an increase in the total damping of the system, resulting in a decrease in the response of the roof.

Therefore, it is necessary to consider the effects of unsteady aerodynamic forces in the wind-resistant design of long-span curved roof with lightweight and low stiffness for evaluating the response of the roof more reasonably.

Author details

Wei Ding

Address all correspondence to: dingwei1985@live.cn

School of Mechanics and Civil Engineering, China University of Mining and Technology, Xuzhou, China

References

[1] Blackmore PA, Tsokri E. Wind loads on curved roof. Journal of Wind Engineering and Industrial Aerodynamics. 2006;**94**(11):833-844

[2] Chen FB, Li QS, Wu JR. Wind effects on a long-span beam string roof structure: Wind tunnel test, field measurement and numerical analysis. Journal of Wind Engineering and Industrial Aerodynamics. 2011;**67**(10):1591-1604

[3] Natalini MB, Morel C, Natalini B. Mean loads on vaulted canopy roof. Journal of Wind Engineering and Industrial Aerodynamics. 2013;**119**:102-113

[4] Wu Y, Chen ZQ, Sun XY. Research on the wind-induced aeroelastic response of closed-type saddleshaped tensioned membrane models. Journal of Zhejiang University: SCIENCE A (Applied Physics & Engineering). 2014;**16**(8):656-668

[5] Yang QS, Wu Y, Zhu WL. Experimental study on interaction between membrane structures and wind environment. Earthquake Engineering and Engineering Vibration. 2010;**9**(4): 523-532

[6] Chen ZQ, Wu Y, Sun XY. Research on the added mass of open-type one-way tensioned membrane structure in uniform flow. Journal of Wind Engineering and Industrial Aerodynamics. 2015;**137**:67-77

[7] Uematsu Y, Uchiyama K. Wind-induced dynamic behaviour of suspended roofs. The Technology Reports of the Tohoku University. 1982;**47**:243-261

[8] Daw DJ, Davenport AG. Aerodynamic damping and stiffness of a semi-circular roof in turbulent wind. Journal of Wind Engineering and Industrial Aerodynamics. 1989;**32**(1–2): 83-92

[9] Ohkuma T, Marukawa H. Mechanism of aeroelastically unstable vibration of large span roof. Wind Engineers, JAWE. 1990;**42**:35-42

[10] Ding W, Uematsu Y, Nakamura M, Tanaka S. Unsteady aerodynamic forces on a vibrating longspan curved roof. Wind and Structures. 2013;**19**(6):649-663

[11] Nozu T, Tamura T. Generation of unsteady wind data in boundary layers and its turbulence structures. In: The 15th National Symposium on Wind Engineering. 1998

[12] Lund TS, Wu X, Squires KD. Generation of turbulent inflow data for spatially-developing boundary layer simulation. Journal of Computational Physics. 1998;**140**(2):233-258

[13] Kataoka H, Mizuno M. Numerical flow computation around 3D square cylinder using inflow turbulence. Journal of Architecture Planning Environment Engineering. 1999;**523**: 71-77

[14] Nozawa K, Tamura T. Large eddy simulation of a turbulent boundary layer over a rough ground surface and evaluation of its fluctuating velocity profile. Journal of Structure and Construction Engineering. 2001;**541**:87-94

[15] Chikamatsu A, Nozawa K, Tamura T. Large eddy simulation of turbulent flows around a cube in an imitated atmospheric boundary layer. In: The 17th National Symposium on Wind Engineering; Tokyo, Japan. 2002

[16] Kondo K, Murakami S, Mochida A. Generation of velocity fluctuations for inflow boundary condition of LES. Journal of Wind Engineering and Industrial Aerodynamics. 1997;**67** & **68**:51-64

[17] Huang SH, Li QS, Wu JR. A general inflow turbulence generator for large eddy simulation. Journal of Wind Engineering and Industrial Aerodynamics. 2010;**98**:600-617

[18] Lu CL, Li QS, Huang SH, et al. Large eddy simulation of wind effects on a long-span complex roof structure. Journal of Wind Engineering and Industrial Aerodynamics. 2012;**100**(1):1-18

[19] Yan BW, Li QS. Inflow turbulence generation methods with large eddy simulation for wind effects on tall buildings. Computers and Fluids. 2015;**116**:158-175